Electrochimica Acta 390 (2021) 138881

Contents lists available at ScienceDirect

Electrochimica Acta

journal homepage: www.elsevier.com/locate/electacta

Hierarchically structured V_2O_3/C microspheres: Synthesis, characterization, and their electrochemical properties

E. Thauer[a,*], G.S. Zakharova[b], L.F. Deeg[a], Q. Zhu[c], R. Klingeler[a,d]

[a] Kirchhoff Institute of Physics, Heidelberg University, Heidelberg, Germany
[b] Institute of Solid State Chemistry, Ural Division, Russian Academy of Sciences, Yekaterinburg, Russia
[c] School of Material Science and Engineering, Wuhan University of Technology, Wuhan, China
[d] Centre for Advanced Materials, Heidelberg University, Heidelberg, Germany

ARTICLE INFO

Article history:
Received 15 March 2021
Revised 1 July 2021
Accepted 1 July 2021
Available online 8 July 2021

Keywords:
Anode material
Composite
Hydrothermal synthesis
Lithium-ion battery
Sphere

ABSTRACT

The V_2O_3/C composites have been successfully synthesized by a facile hydrothermal thermolysis method, employing vanadyl hydroxide as precursor and different carboxylic acids as both a carbon source and reducing agents. The morphology, structure, and composition of the obtained V_2O_3/C composites were investigated by X-ray diffraction, Raman spectroscopy, scanning and transmission electron microscopies, physical sorption, thermogravimetric analysis coupled with mass-spectrometry, and elemental analysis. The as-prepared V_2O_3/C composites consist of hierarchically structured microspheres, either with core-shell or solid architecture depending on the used carboxylic acid. When used as anode for lithium-ion batteries, the V_2O_3/C spheres deliver very good electrochemical performance with high specific capacity, great cyclic stability, and high rate capability. The large capacitive current contribution favors superior lithium storage kinetics compared to more compact chunk-shaped V_2O_3/C materials. In particular, the composite prepared with tartaric acid exhibits a high reversible capacity of 454 mAh g^{-1} after 100 cycles at 100 mA g^{-1}.

1. Introduction

Nowadays, rechargeable lithium-ion batteries (LIB) are the most promising energy storage systems for mobile applications, including electric vehicles, due to their high energy density, high energy efficiency and long cycle life [1–5]. It is well-known that the electrode materials play a decisive role in determining the LIBs performance. Graphite, the predominant commercial anode material, has a rather low theoretical capacity of 372 mA h g^{-1}, that cannot meet the ever-growing demand for next generation high energy LIBs [6,7]. Thus, in recent years, many endeavours have been placed on exploring alternative anode materials for LIBs, especially transition metal oxides have attracted intense research in view of their high theoretical capacities [8–13]. Among them, vanadium trioxide (V_2O_3) is favoured for its high theoretical capacity (1070 mA h g^{-1}), low working potential, low cost, natural abundance, and environment friendliness [14–17]. Particularly, it undergoes a first order metal-to-insulator transition at 150–160 K accompanied by a change from a paramagnetic rhombohedral phase into an antiferromagnetic monoclinic phase [18,19]. So, V_2O_3 exhibits moderate electronic conductivity at room temperature, which is much higher than that of other transition metal oxides, such as MnO_2, Fe_2O_3, Co_3O_4 [20]. However, its poor cycling stability seriously hinders its practical application. Vanadium trioxide suffers from large volume change during Li-ion insertion/extraction resulting in cracking and pulverization. To overcome this issue, rational structure design and the preparation of composites with carbonaceous materials have proven to be promising strategies in recent years [21]. Building hierarchical nano-/micro-architectures can combine both the advantageous of nanosized primary particles and micro-sized arrangements [22–24]. Nanomaterials can accommodate large mechanical strain of Li-ion insertion/extraction improving the cycle life and, in addition, possessing high specific surface area and short Li^+ diffusion path leading to high energy and power density [25,26]. Hierarchical structures guarantee structural stability by preventing agglomeration of the nanoparticles, which occurs due to low thermodynamic stability [24,27]. When using carbonaceous materials for the stabilising matrix, carbon can serve, on the one hand, as a buffer to accommodate changes in volume and as a physical barrier to prevent the agglomeration and restacking of V_2O_3 particles on the other [28,29]. Moreover, the carbon can effectively improve the electronic conductivity by forming a conductive network [14,30].

* Corresponding author.
E-mail address: elisa.thauer@kip.uni-heidelberg.de (E. Thauer).

https://doi.org/10.1016/j.electacta.2021.138881
0013-4686/

Table 1
The molecular structure and acid dissociation constant of the selected carboxylic acids.

Carboxylic acid	Chemical formula	Structure	Acidity (pK_{a1})
Citric acid	$C_6H_8O_7$	fx	3.13
Malic acid	$C_4H_6O_5$	fx	3.46
Tartaric acid	$C_4H_6O_6$	fx	3.04

For example, dandelion-like V_2O_3/C composite with bicontinuous 3D hierarchical structures, which was synthesized by a template-free solvothermal method, shows high reversible capacity, outstanding cycling performance and excellent rate capability [31]. Yu et al. [32] reported that urchin-like V_2O_3/C hybrid composed of nanofibers and hollow nanospheres delivered a discharge capacity of 737 mA h g^{-1} after 100 cycles at a current density of 0.1 A g^{-1}. Jiang et al. [33] prepared via a template-free polyol solvothermal method carbon-coated V_2O_3 yolk−shell microspheres. The hierarchically structured V_2O_3/C composite shows superior electrochemical performance compared to bulk V_2O_3. Liu et al. [34] fabricated 3D hierarchical porous V_2O_3@C micro/nanostructures consisting of crumpled nanosheets through self-reduction under annealing from the structurally similar VO_2(B)@C precursor exhibiting a large reversible capacity up to 732 mA h g^{-1} at 100 mA g^{-1} even after 136 cycles.

Herein, we report for the first time the hydrothermal method with the post-annealing treatment to synthesize a V_2O_3/C composite material with a unique hierarchical structure using citric acid, tartaric acid, and malic acid as both the carbon sources and reducing agents. The chosen organic acids possess different molecular structure, acidity affecting the hydrolysis reaction, and different numbers of hydroxyl groups as well as carboxyl groups which can serve as organic ligands in the coordination reaction with vanadium ion. The chemical formula of used carboxylic acids and their molecular structure are summarized in Table 1. The influence of the synthesis conditions on the chemical composition, morphology, texture, and electrochemical properties of V_2O_3/C composites is particularly investigated.

2. Experimental

2.1. Materials

Vanadyl sulfate hydrate $VOSO_4 \bullet nH_2O$ (97% $VOSO_4$), ammonium hydroxide solution (28% NH_3 in H_2O), tartaric acid ($C_4H_6O_6$), malic acid ($C_4H_6O_5$), and citric acid ($C_6H_8O_7$) with analytical grade were purchased from Sigma–Aldrich and used without any further purification.

2.2. Synthesis of V_2O_3/C composites

V_2O_3/C composites were prepared using the hydrothermal thermolysis process. The typical synthesis route is briefly described as follows. Firstly, vanadyl hydroxide $VO(OH)_2$ precursor was prepared. According to the synthetic procedure, 7.95 g $VOSO_4 \bullet nH_2O$ was dissolved in 400 mL of deionized H_2O using magnetic stirring at room temperature, then ammonium hydroxide solution was added dropwise (one drop every ~1 min) to adjust the pH value of the mixture equal to 4 The brown precipitate was collected by centrifugation, washed several times with water and ethanol, and dried at 25 °C in air to obtain the $VO(OH)_2$ powder products. Secondly, $VO(OH)_2$ and the carboxylic acid (citric acid, malic acid or tartaric acid) were weighed in at a molar ratio of 1: 1 and mixed well together in deionized 60 mL water under constant stirring. The mixture became a clear-blue solution, which was then transferred to a 45 mL stainless steel autoclave lined with PTFE. The autoclave was heated at 180 °C for 24 h and then cooled to room temperature naturally. The obtained product was filtered, washed with deionized water, and dried in air under ambient conditions. Finally, the powder was sintered under a flow of N_2 gas at 400–650 °C for 1 h to obtain the V_2O_3/C composites. Depending on the type of the carboxylic acids, the resulting materials are termed below as V_2O_3/C-C (citric acid), V_2O_3/C-M (malic acid), and V_2O_3/C-T (tartaric acid).

2.3. Characterization

Powder X-ray diffraction (XRD) in the 10–70 ° 2θ range with a step size of 0.2 ° was performed on a Bruker AXS D8 Advance Eco diffractometer using CuKα radiation. The morphology of the samples was investigated by a ZEISS Leo 1530 scanning electron microscope (SEM) and a JEOL JEM 2100 transmission electron microscope (TEM). The energy dispersive X-ray analysis was performed on JEOL JSM 6390 LA scanning electron microscopy equipped with an EX-23010BU energy-dispersive X-ray analyzer. Raman spectra were measured with an inVia Reflex spectrometer (Renishaw) using a 100 mW RL532–08 solid state laser with a 532 nm wavelength. To avoid damages of the samples, the emitted power was decreased up to 1%. Thermogravimetric analysis (TG-DSC-MS) with a heating rate of 10 K•min^{-1} starting from room temperature up to 750 °C under flowing air was carried out using STA 449 F_3 Jupiter thermoanalyzer (Netzsch) coupled with a QMS 403 mass spectrometer. The textural characteristics (specific surface area, porosity) of the samples were determined with a Gemini VII (Micromeritics) analyzer on the basis of low-temperature nitrogen adsorption. The samples were prepared by evacuation at 100 °C for 3 h. The specific surface area was calculated by the Brunauer–Emmett–Teller (BET) method using nitrogen adsorption isotherms. The pore-size distribution curves were calculated by the Barrett–Joyner–Halenda method. The content of carbon was determined by CHN elemental analysis (EA) using Vario MICRO Cube (Elementar).

2.4. Electrochemical measurements

Electrochemical studies were performed with a VMP3 potentiostat (Bio-Logic SAS) at 25 °C using Swagelok-type half cells with lithium metal foil (Alfa Aesar) pressed on a nickel current collector as counter electrode (see [35]). The working electrode consists of 75 wt% active material, 15 wt% carbon black (Super C65, Timcal) and 5% polyvinylidene fluoride binder (Solvay Plastics) and were prepared as follows. First, the powders were mixed in N-methyl-2-pyrrolidone (NMP, Sigma-Aldrich) and stirred for at least 12 h. To obtain a spreadable slurry most of the NMP was evaporated under vacuum. Afterwards, the electrode slurry was applied on circular Cu meshes (wire diameter: 0.115 mm, nominal aperture: 0.14 mm, wires/inch: 100 × 100, open area: 30.3%, thickness: 0.25 mm,) with 10 mm diameter and the resulting electrodes were dried under vacuum, pressed with a spindle press by hand and then dried again. The electrodes were separated by two glass fiber layers (Whatman GF/D). As electrolyte 200 μl of a 1 M $LiPF_6$ salt solution in 1:1 ethylene carbonate and dimethyl carbonate (Merck Electrolyte LP30) was used. The preparation of the electrodes and the cell assembly were done in a glovebox filled under argon atmosphere (O_2/H_2O < 5 ppm). For *ex-situ* SEM measurement, the cells were galvanostatically cycled at 100 mA g^{-1} and disassembled in the glove box. The electrodes were washed in DMC and dried under vacuum conditions. The calculation of the specific capacity is based on the total mass weight of the composites V_2O_3/C.

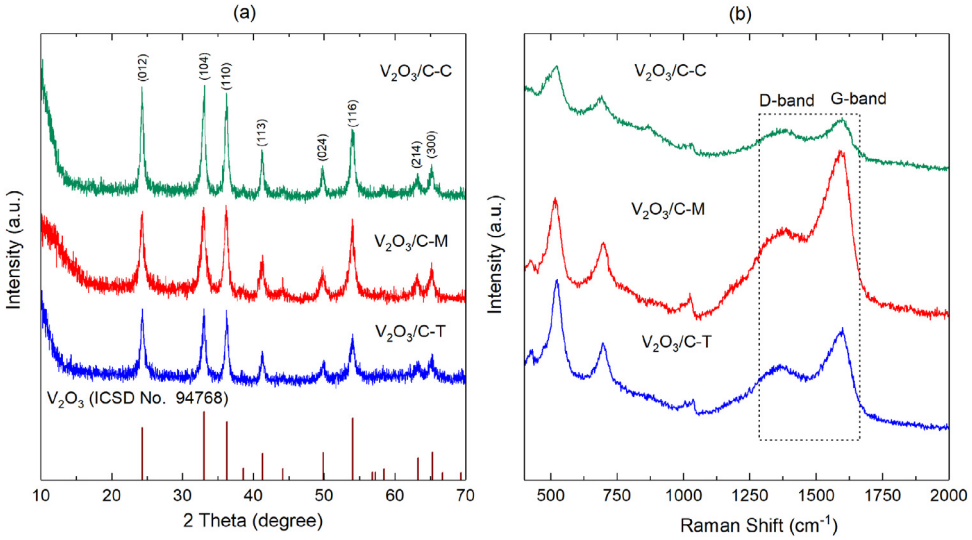

Fig. 1. (a) XRD patterns and (b) Raman spectra of the V_2O_3/C composites fabricated using different carboxylic acids: citric acid (V_2O_3/C-C), tartaric acid (V_2O_3/C-T), and malic acid (V_2O_3/C-M). In addition, the ICSD #94,768 [36] reference pattern of rhombohedral V_2O_3 is shown in (a).

Table 2
Crystallite sizes from XRD, results of the BET analysis, and carbon content of the V_2O_3/C composites.

Samples	Crystallite size (nm)	S_{BET} ($m^2 \bullet g^{-1}$)	Carbon content (wt%) TG	EA
V_2O_3/C-C	17(2)	27.2	6.0	6.5(5)
V_2O_3/C-M	14(2)	34.5	13.0	12.5(5)
V_2O_3/C-T	16(2)	90.0	12.6	12.6(5)

3. Results and discussion

Fig. 1a shows the XRD patterns of the V_2O_3/C composites synthesized using different carboxylic acids. The samples obtained using malic acid and tartaric acid after hydrothermal treatment but before annealing in inert atmosphere are XRD amorphous samples (Fig. S1). On contrary, XRD pattern of the citric acid-assisted sample after hydrothermal treatment shows a low crystallinity of the compound. It can be explained by the stronger redox activity of citric acid. Annealing at 650 °C leads to the appearance of distinguished XRD patterns, which can be assigned to the rhombohedral V_2O_3 phase according to ICSD #94,768 [36]. No impurity peak can be observed, which demonstrates the successful synthesis of phase pure V_2O_3. The average crystallite sizes of V_2O_3 in the V_2O_3/C-composites can be estimated using the Scherrer equation:

$$D_{hkl} = K\lambda/\Delta(2\theta_{hkl})cos\theta_{hkl}, \quad (1)$$

where D_{hkl} is the average grain size based on the particular reflecting crystal face (hkl) direction, K is a shape factor which can be approximated to 0.9, λ is the wavelength of the applied Cu Kα radiation, $\Delta(2\theta_{hkl})$ is the full width at half-maximum of the diffraction peak, and θ_{hkl} is the Bragg angle. The averaged crystallite sizes of V_2O_3 in the composites V_2O_3/C-C, V_2O_3/C-M and V_2O_3/C-T obtained from the analysis of the (012), (104), (110), and (116) reflexes are listed in Table 2. We conclude that the composites exhibit V_2O_3 nanoparticles which crystallite size does not distinctly depend on the choice of carbon source. In addition, the different Bragg peaks yield very similar results which suggests rather regularly shaped particles.

To confirm the composite formation between V_2O_3 and carbon component, Raman analysis was carried out (Fig. 1b). It can be observed that two typical broad peaks, corresponding to the D- and G-bands, are located at about 1361 and 1595 cm^{-1}. The D-band is associated to the breathing mode of sp^2 hybridized carbon atoms in rings and only becomes active in the presence of defects and disordering atomic arrangements in the hexagonal graphitic layers. The G-bands corresponds to the in-plane vibration of sp^2-bonded carbon atoms [37]. Additionally, the pointed peaks are broad, indicating the presence of amorphous carbon with a low crystallinity. The ratio of the maximum intensities of these peaks, I_D/I_G, was calculated as 0.73, 0.77 and 0.88 for V_2O_3/C-M, V_2O_3/C-T and V_2O_3/C-C composites, respectively. As for the peaks below 1100 cm^{-1}, they are attributed to V–O vibrations as described in previous V_2O_3-based reports [38]. It should be noted that the Raman spectra for samples obtained after hydrothermal treatment but before annealing in inert atmosphere (Fig. S1) do not contain carbon typical vibrational modes.

The elemental chemical analyses of the composites yield a carbon content of 12.5(5)% and 12.6(5)% for V_2O_3/C-M and V_2O_3/C-T, respectively, and thus about twice as much as for the composite prepared with citric acid with 6.5(5)% carbon (see Table 2).

The morphology and topography of the V_2O_3/C composites synthesized using citric acid, malic acid, and tartaric acid as both carbon source and reducing agent were investigated by SEM (Fig. 2) and TEM measurements (Fig. S2). It is observed that all of them show hierarchically structured spheres with diameters about 1–4 µm. Some microspheres are connected to each other. The SEM images of citric acid and malic acid assisted V_2O_3/C composites display core-shell structures filled with a solid core. The thickness of the shells is about 200–300 nm. Obviously, the topography of the samples is affected by the carboxylic acid. The shells of the V_2O_3/C-C composite prepared using citric acid consist of nanoparticles with a size of only a few 10 nm, resulting in a rough surface texture with very fine granulation (Fig. 2 a and b). In the composite V_2O_3/C-M prepared using malic acid the shell has a coarse-grained surface to which particles with varying size up to 300 nm are attached (Fig. 2 c and d). In contrast to V_2O_3/C-C and V_2O_3/C-M composites, the SEM images of the broken microspheres of tartaric acid assisted V_2O_3/C-T composite reveal the solid interior structure (Fig. 2 e and f). It can be seen that the solid microspheres are composed of closely packed nanoparticles with the average size of about 25–40 nm, while the surface is decorated with flake-like nanoparticles. The core-shell structure of the V_2O_3/C composites prepared using citric acid and malic acid is confirmed by TEM measurements (Fig. S2 a–c). In the high resolution TEM image of V_2O_3/C-M composite a lattice spacing of 0.362 nm is mea-

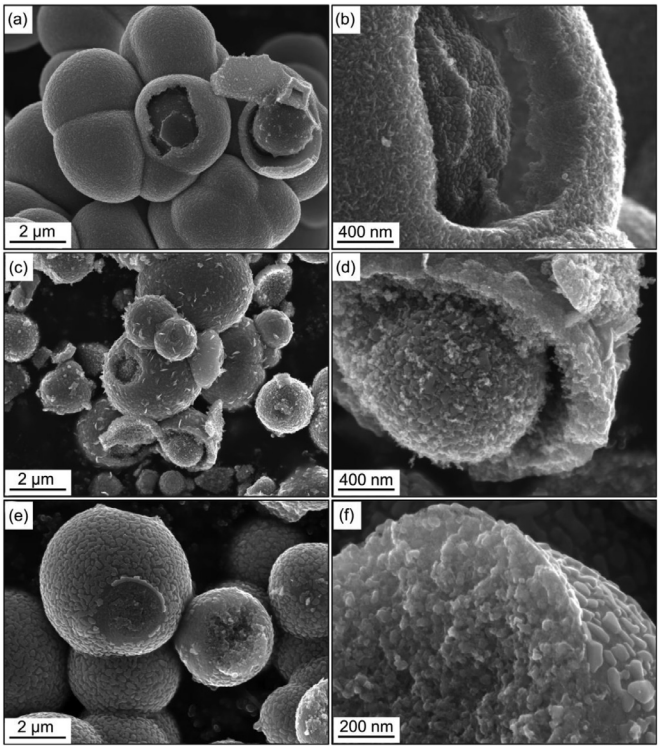

Fig. 2. SEM images of V_2O_3/C composites prepared using the different carboxylic acids: (a,b) citric acid, (c,d) malic acid, and (e,f) tartaric acid.

sured corresponding to the (012) crystal plane of rhombohedral-phase crystalline V_2O_3 (Fig. S2 d). Selected area electron diffraction (SAED) confirms the crystalline structure of V_2O_3 in the V_2O_3/C composite (Fig. S2 e). The observed Debye-rings in the SAED pattern can be indexed to the rhombohedral phase of V_2O_3, with diffraction rings corresponding to the (012), (104), (110), (020), (113), (116), and (300) crystal planes from inner to outer. Our data reveal the crucial role of the carboxylic acids on the morphology and internal microstructure of the resultant V_2O_3/C composites. The morphological structure of the composites prepared using citric acid and malic acid significantly differs from that of V_2O_3/C synthesized using tartaric acid. It is found that the formation the core-shell structure is a time-dependent process [33,39]. In the initial state of the process, the nanoparticles are assembled to spherical solid aggregates by the coordination reaction of the vanadium ion with organic ligand caused by the hydrogen bond and van der Waals interaction [31]. With increasing reaction time, spherical aggregates grow by the deposition of sheet-like particles on the surface of these aggregates. On prolonging the hydrothermal time, the solid microspheres evolve to microspheres with core-shell structure due to an inside-out Ostwald-ripening process that involves the dissolution of the unstable inner core and subsequent recrystallisation at the outer surface to form shells with a more stable phase [40]. The formation mechanism of core-shell structures establishes that the primary seed concentrations play a key role in the crystal nucleation and growth. It is known that the fast hydrolysis rate, which is inversely proportional to the dissociation constant of the compound, produces more primary particles [41]. In the case of V_2O_3/C composites, the primary particles are formed by hydrolysis of VO^{2+}-carboxylic acid complex using the water molecules as solvent. For citric acid, malic acid, and tartaric acid, the negative logarithm of the acid dissociation constant (pK_{a1}) is 3.13, 3.46, and 3.04, respectively. Accordingly, the stronger tartaric acid provides a lower degree of hydrolysis and fewer primary particles obtained. The low density of primary particles requires more time for them to assemble into spherical aggregates with a core-shell structure. In the case of V_2O_3/C-T composite (Fig. 2e), the hydrothermal treatment for 24 h only results in the deposition of the outer shell on the surface of cores which is the second stage of the formation of the core-shell microspheres. The elemental mapping analysis of V_2O_3/C-C composite, selected as an example, confirms the coexistence and homogeneous dispersion of V, O, and C elements (Fig. S3).

In order to determine the carbon content of V_2O_3/C composites, TG-DSC-MS measurements of the as-prepared samples were carried out under air flow. It can be observed that several steps emerge from the TG-curves of the V_2O_3/C composites (Fig. 3). In all samples, the first step starts from about 70 °C and ends at 200 °C. It can be mainly attributed to the loss of water absorbed on the material's surface. The process is accompanied by a very weak and broad endothermic peak centered at about 90 °C. The next weight loss from 200 °C up to ~400 °C is caused by the oxidation of the carbon component of the V_2O_3/C composites and the emission of CO_2 gases (m/z = 44 a.m.u.) as corroborated by the analysis of the MS-curves (ion current versus temperature). For the V_2O_3/C-C composite, this process is described by two distinct steps of weight loss which can be attributed to a successive oxidation of the carbon component, first of the carbon shell and then of the carbon core of the sphere-like particles (Fig. 3a). Additionally, the TG-curve for V_2O_3/C-C composite shows a small mass increase (0.3 wt%) from 357 to 384 °C originating from the oxidation of the outer V_2O_3. While the carbon shell is oxidized, the outer V_2O_3 becomes exposed to air and oxidizes to V_2O_5. The combustion reactions of the carbon component in V_2O_3/C-C composite are accompanied by two broad exothermic peaks in the DSC-curves centered at 354 and 408 °C. A large exothermic peak width indicates that the reactions occur at a low rate. For V_2O_3/C-M composite, the results imply removal of carbon within two distinct steps as indicated by one pronounced peak at around 396 °C and the visible satellite peak at about 360 °C in the MS-curve (Fig. 3b). This process is accompanied by one broad exothermal peak in the DSC-curve at 392 °C. The thermal behavior of the V_2O_3/C-M composite is similar to the one of the acid-assisted composite as it also reflects the particular core-shell morphology (Fig. 2c and d). In contrast, in the case of V_2O_3/C-T composite exhibiting a solid interior structure, the decomposition of the carbon component by oxidation and the release of CO_2 gases occurs within only one stage (Fig. 3c). A strong and sharp exothermal peak with its maximum at 384 °C is observed indicating the vigorous combustion reaction of the carbon. According to the TG-curves, the calculated carbon contents in V_2O_3/C-C, V_2O_3/C-M and V_2O_3/C-T composites amount to 6.0 wt%, 13.0 wt%, and 12.6 wt%, respectively. These results are in a good agreement with the results of the carbon content determination by the EA (Table 2). The last step in the TG curves ranging from ~400 to 750 °C shows a weight gain of about 0.2 wt%, 1.3 wt% and 3.1 wt% for V_2O_3/C-C, V_2O_3/C-M, and V_2O_3/C-T, respectively. This process is attributed to the full oxidation of V^{3+} ions to V^{5+} resulting in the formation of V_2O_5 as a final thermolysis product. From the mass spectroscopy curves it is evident that the main gaseous product is the molecular ion O_2^+ with m/z = 32 a.m.u., whose content changes during this process. A sharp endothermic peak at ~677 °C in the DSC-curves can be ascribed to the melting of V_2O_5.

The texture properties of the composites were investigated by nitrogen sorption isotherms (Fig. 4). All measured curves can be classified as a type-IV isotherm which is typical for mesoporous materials [42]. Unlike V_2O_3/C-M and V_2O_3/C-T, an H3 hysteresis loop occurs in V_2O_3/C-C at high relative pressures (P/P_0 = 0.7–0.9), indicating the presence of macropores (Fig. 4a). Specifically, the H3 hysteresis loop testifies about the presence of the aggregated plate-like particles with slit-shaped pores structure [42]. Both V_2O_3/C-M

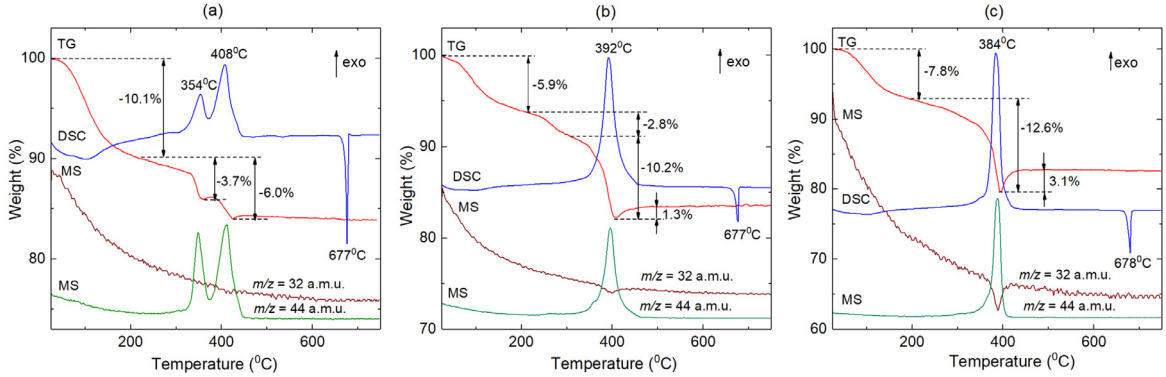

Fig. 3. Thermogravimetric (red), DSC (blue), and mass spectroscopy (brown, green) curves of V_2O_3/C composites prepared using (a) citric acid, (b) malic acid, and (c) tartaric acid (For interpretation of the references to color in this figure legend, the reader is referred to the web version of this article).

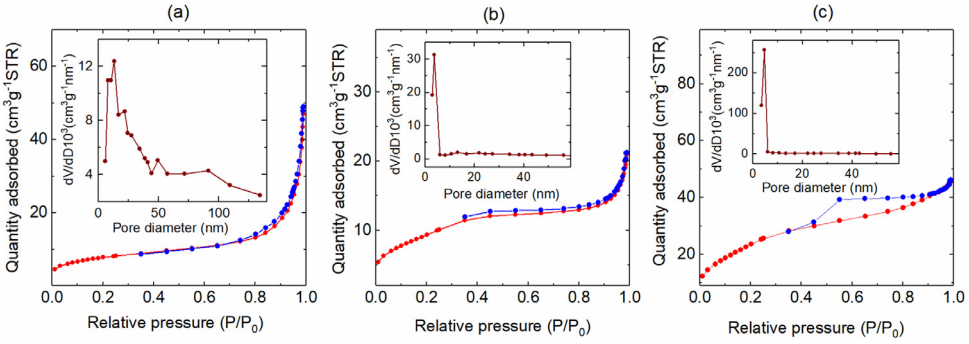

Fig. 4. Nitrogen sorption isotherms and corresponding pore-size distributions (inset) of V_2O_3/C composites prepared using (a) citric acid, (b) malic acid, and (c) tartaric acid.

and V_2O_3/C-T samples exhibit type H4 loops associated with narrow slit-like pores (Fig. 4b and c). The BET specific surface areas of the V_2O_3/C composites are displayed in Table 1. In comparison with V_2O_3/C-C and V_2O_3/C-M, the BET surface area of the V_2O_3/C-T composite is rather high which may be due to the particular morphology of this material (see Fig. 2). For V_2O_3/C-M and V_2O_3/C-T composites, the pore-size distribution is monomodal with the predominant size of about 4 nm (Fig. 4b and c, inset) while, in contrast, V_2O_3/C-C composite exhibits an inhomogeneous pore structure. The pore-size distribution for V_2O_3/C-C composite is observed in a wide range, demonstrating the co-existence of both mesopores and macropores (Fig. 4a, inset). These differences in the textural properties are caused by using of various carboxylic acids as the carbon source. The inhomogeneous pore structure of V_2O_3/C-C might arise from the microcracking of the sample by a large amount of gases generated in the heating of the V-O precursor with citric acid leading to a wide size distribution. Compared to malic acid and tartaric acid, citric acid has the highest molecular mass favoring the release of a large amount of gases during the post-annealing treatment (H_2O, CO_2, O_2, CO).

The electrochemical properties of the V_2O_3/C composites are investigated by cyclic voltammetry (CV) and galvanostatic cycling with potential limitation (GCPL) within the potential window between 0.01 and 3.2 V. Fig. 5a displays the first, second, and fifth cycle of the cyclic voltammogram of V_2O_3/C-C recorded at a scan rate of 0.05 mV s^{-1}. As the comparison of the CV curves of the other two composites V_2O_3/C-M and V_2O_3/C-T (Fig. S4) shows, there are no pronounced differences between the composites prepared with different carboxylic acids. During the first reductive scan, there is a peak at around 0.75 V which disappears in the subsequent cycles, corresponding to the irreversible formation of a solid electrolyte interface (SEI) from the decomposition of electrolyte [14]. The storage of Li-ions in the carbonaceous structures is reflected by the redox activity around the lower voltage limit 0.01 V [43]. The remaining redox activity can be assigned to the electrochemical lithiathion/delithiation mechanism of V_2O_3, that can be described as follows [44,45]:

$$V_2O_3 + xLi^+ + xe^- \leftrightarrow Li_xV_2O_3, \quad (2)$$

$$Li_xV_2O_3 + (6\text{-}x)Li^+ + (6\text{-}x)e^- \leftrightarrow 2\ V + 3Li_2O. \quad (3)$$

During discharge, Li^+ are firstly intercalated into V_2O_3 to form $Li_xV_2O_3$ (Eq. (2)). While more Li-ions are inserted, Li_2O is formed by a conversion reaction accompanied by the total reduction of the vanadium (Eq. (3)). The charge process follows the reverse reactions. Due to the multivalency of vanadium, several transition states can coexist during the dis-/charge process leading to the observed smooth course of the CV curves without pronounced peaks [14,46]. The second and fifth CV cycles are mostly overlapped, implying high reversibility of the Li^+ storage in the hierarchically structured V_2O_3/C sphere electrode.

GCPL measurements enable to investigate the cycling behavior of the V_2O_3/C composites as an anode material for lithium-ion batteries. Fig. 5b shows the dis-/charge capacities at 100 mA g^{-1} for the first 100 cycles. For comparison, the data of V_2O_3/C microparticles with chunk-shaped morphology (V_2O_3/C-C-SG) synthesized by a sol-gel process, which were reported in detail elsewhere [47], are also shown. The potential profiles exemplarily shown for V_2O_3/C-C in Fig. 5c are fully consistent with the CV measurements. During galvanostatic cycling the potential gently decreases and no obvious plateaus appear, indicating that V_2O_3 reacts smoothly with Li-ions. While there are no major differences to the other two composites V_2O_3/C-M and V_2O_3/C-T in the potential profiles (Fig. S5), clear differences can be observed in the reached capacities. In the first cycle, specific dis-/charge capacities of 680/380 mAh g^{-1} and

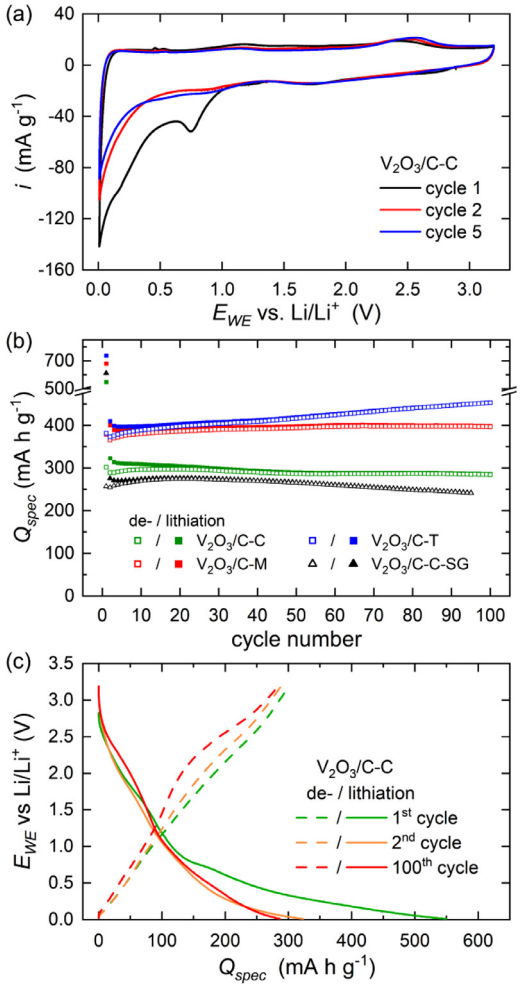

Fig. 5. (a) CV curves of V_2O_3/C-C recorded at a scan rate of 0.05 mV s^{-1}. (b) Specific dis-/charge capacities for the composites fabricated by hydrothermal thermolysis method using citric acid (V_2O_3/C-C), malic acid (V_2O_3/C-M), tartaric acid (V_2O_3/C-T), and by citric acid-assisted sol-gel method (V_2O_3/C-C-SG) during galvanostatic cycling at 100 mA g^{-1} and (c) corresponding potential profiles of the first, second and hundredth cycle for the V_2O_3/C-C composite.

738/381 mAh g^{-1} are measured for V_2O_3/C-M and V_2O_3/C-T, respectively, and only 549/302 mAh g^{-1} for the composite V_2O_3/C-C. The irreversible capacity in the initial cycle originates from the SEI formation and structural changes during the first lithiation as observed in the CV curves [15,16,44]. In comparison to the composites V_2O_3/C-M and V_2O_3/C-T, the composite V_2O_3/C-C has only about half the carbon content and the smallest surface area which might explain the lower capacity. All three composites exhibit excellent capacity retention. After 100 cycles the composites V_2O_3/C-M and V_2O_3/C-T reach discharge capacities of 399 and 454 mAh g^{-1}. The composite V_2O_3/C-C still achieves 284 mAh g^{-1}. Even an increase of the capacity with cycling can be observed for V_2O_3/C-M and V_2O_3/C-T and for the composite V_2O_3/C-C at least in the first twenty cycles. This is also reported in the literature and can be attributed to an activation process resulting from the electrochemical grinding effect [14,16,34,51]. The progressive particle pulverization leads to the exposure of inner inactive regions and thus generates new active sites for electrochemical reactions. The results of the galvanostatic dis-/charge measurements suggest that the morphological structure, core-shell microspheres as for V_2O_3/C-M or solid microspheres as for V_2O_3/C-T, does not seem to affect the electrochemical performance. In addition, it is clearly observed that in comparison to the chunk-shaped composite V_2O_3/C-C-SG (specific

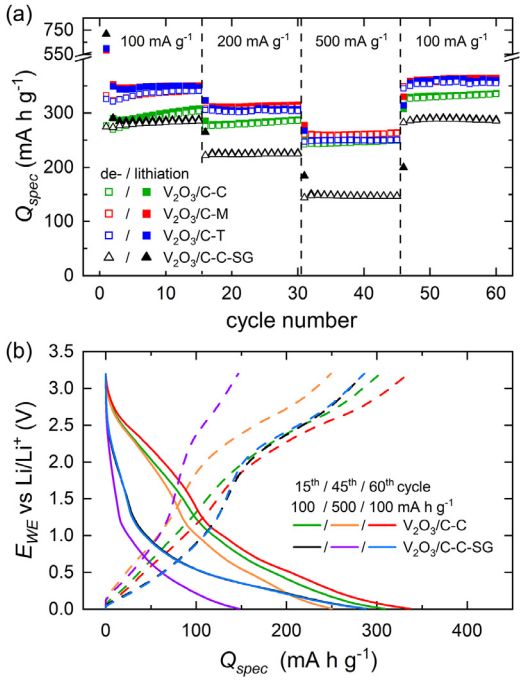

Fig. 6. (a) Specific charge/discharge capacities of rate capability test with different cycling rates between 100 and 500 Ma g^{-1} and (b) corresponding potential profiles of the composites prepared by hydrothermal synthesis using citric acid (V_2O_3/C-C), and the composite V_2O_3/C-C-SG fabricated by citric acid-assisted sol-gel method.

surface area of 1.8 m^2 g^{-1} [47]) fabricated by citric acid-assisted sol-gel method the composites prepared by hydrothermal synthesis exhibit superior electrochemical performance. The composites with sphere-like morphology achieve higher specific capacities with enhanced cycling stability which might be attributed to their special architecture and larger specific surface area. SEM images (Fig. S6) of V_2O_3/C-C electrodes, selected as an example, after 1 cycle and after 200 cycles confirm the structural stability of the hierarchically structured V_2O_3/C microspheres during cycling. The chunk-shaped V_2O_3 may suffer from structural degradation and self-aggregation during cycling, which results in poor cycling stability.

The results of the rate capability studies at current densities from 100 to 500 mA g^{-1} are shown in Fig. 6. Among all samples, the composite V_2O_3/C-M prepared using malic acid, exhibits the best performance with specific discharge capacities of 351 mAh g^{-1}, 316 mAh g^{-1} and 263 mAh g^{-1} at rates of 100 mA g^{-1}, 200 mA g^{-1}, and 500 mA g^{-1} after 15 cycles each, corresponding to a capacity retention of 75% when increasing the current by five times. Moreover, when the current density is returned to 100 mA g^{-1} the original capacity is fully recovered, demonstrating a remarkably high rate capability. The other two samples also show high rate performance while, the composite V_2O_3/C-C-SG exhibits much lower capacities, at all measured current rates in comparison, further confirming the beneficial properties of the sphere-like structure of the samples V_2O_3/C prepared via citric acid, malic acid, or rather tartaric acid-assisted hydrothermal thermolysis method. The potential profiles in Fig. 6b show for the composite V_2O_3/C-C-SG the higher overpotential in terms of lower discharge and higher charge potential with increasing rate which results from kinetic effects.

To explain the superior rate performance of the porous sphere-like composites compared to chunk-shaped V_2O_3/C, the surface-induced capacitive and diffusion-controlled processes were quantified by studying the lithium storage kinetics. Fig. 7a and b show the CV curves of V_2O_3/C-C and V_2O_3/C-C-SG at scan rates ranging

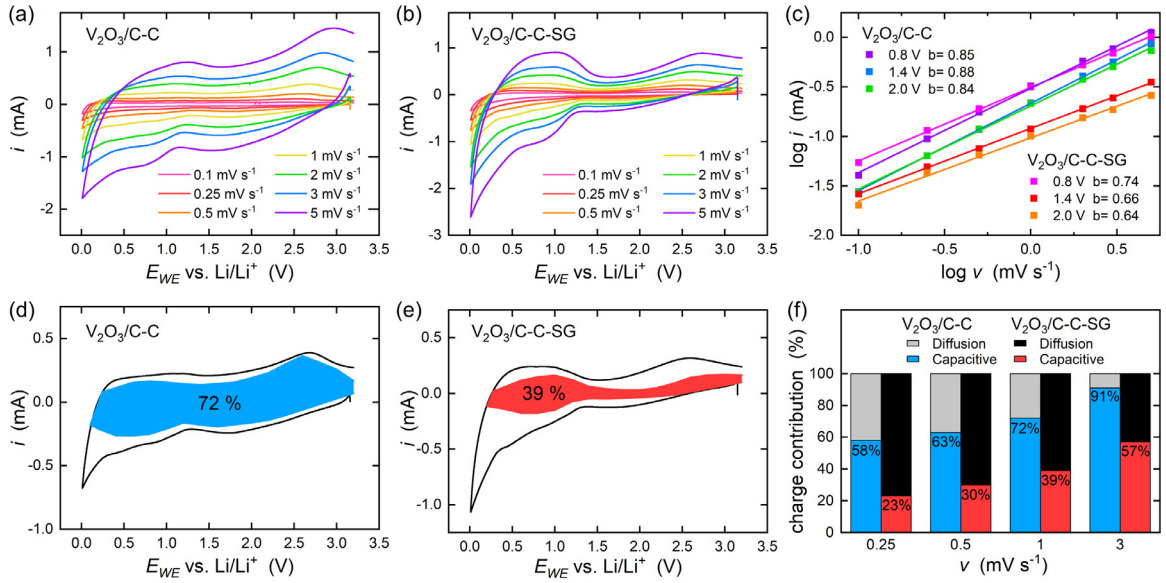

Fig. 7. Kinetic analysis: CV curves at different scan rates of (a) V_2O_3/C-C and (b) V_2O_3/C-C-SG. (c) Power law dependence of current response on scan rate at various potentials for reductive sweep. Capacitive contribution (shaded area) to the total current at a scan rate of 1 mV s^{-1} of (d) V_2O_3/C-C and (e) V_2O_3/C-C-SG. (f) Normalized contribution ratio of capacitive and diffusion-controlled charge storage at different scan rates.

Table 3
Comparison of the electrochemical performance of V_2O_3/C electrodes prepared via solvo- and hydrothermal synthesis as reported in the literature.

Material	Current density (mA•g^{-1})	1st charge capacity (mAh•g^{-1})	Specific capacity (mAh•g^{-1})/cycle no.	Refs.
Core-shell V_2O_3/C nanoplatelets	100	360[a]	260/100	[29]
Yolk-shell V_2O_3/C microspheres	100	470[a]	437.5/100	[33]
V_2O_3/C nanoparticles	200	380	525/200	[16]
Dandelion-like V_2O_3/C spheres	500	280[a]	474/400	[31]
Peapod-like V_2O_3/C nanowires	100	230	186/125	[54]
Core-shell V_2O_3/C microspheres	100	380	399/100	This work
Solid-structured V_2O_3/C microspheres	100	381	454/100	This work

[a] Values are estimated from the graphs.

from 0.01to 5 mV s^{-1} for one cycle each starting with the second cycle. The relationship of current (i) and scan rate (v) obeys the power law formula

$$i = av^b, \tag{4}$$

where both a and b are adjustable values [48,49]. A b value of 0.5 indicates a totally diffusion-controlled process, while for an ideal capacitive process the b value is 1 [49,50]. By plotting log(i) vs. log (v), the b value can be obtained from the slope. Fig. 7c shows the b values of V_2O_3/C-C and V_2O_3/C-C-SG at various potentials for reductive sweep. The higher b values calculated for V_2O_3/C-C compared to V_2O_3/C-C-SG suggest a higher capacitive contribution in the V_2O_3/C-C composite. Quantitatively, the capacity contribution of the current response can be determined by using the following equation [51,52]:

$$i(V) = k_1v + k_2v^{1/2}. \tag{5}$$

The current at a fixed potential V can be divided into two parts, one originating from the capacitive effects (k_1v) and one from diffusion-controlled processes ($k_2\ v^{1/2}$). By plotting $i(V)/v^{1/2}$ vs. $v^{1/2}$, k_1 and k_2 at a certain potential can be determined by the slope and the y-axis intercept (Fig. S7). The kinetic analysis at 1 mV s^{-1} reveals that the Li^+ storage for V_2O_3/C-C is more determined by capacitive effects than for V_2O_3/C-C-SG. As shown in Fig. 7d, 72% of the total charge of V_2O_3/C-C results from capacitive processes (highlighted by the shaded area), while for V_2O_3/C-C-SG it is only 39% (Fig. 7e). A high fraction of capacitive charge storage is very advantageous since surface-induced processes are much faster than diffusion-controlled processes, and thus explains the excellent rate capability of V_2O_3/C-C. Furthermore, it causes smaller volume changes during de-/lithiation compared to diffusion-controlled processes resulting in an improved cycling stability [53]. We attributed these high capacitive contributions to the large surface area of V_2O_3/C-C spheres. As expected, with an increasing scan rate, increasing capacitive contributions were obtained (Fig. 7f). This can be explained by the slower Li^+ diffusion compared to the faster and less rate-depended contribution of the surface-induced capacitive processes.

The results of this study clearly indicate that the V_2O_3/C composites with sphere-like structure exhibit an enhanced electrochemical performance as compared to chunk-like V_2O_3/C. Moreover, as demonstrated by Table 3, the composite V_2O_3/C spheres also compete well with other V_2O_3/C materials prepared via solvo- or hydrothermal synthesis reported in literature. The excellent charge storage performance of the hierarchically structured V_2O_3/C microspheres can be attributed to their special architecture in several aspects. As above mentioned, the hierarchical assembly of nanoparticles may offer many advantages, including improved structural stability of the electrode material. Compared to V_2O_3/C chunks, the porous V_2O_3/C microspheres have a larger specific surface area, which shortens the diffusion path of Li-ions and increases the number of electrochemical active reaction sites. Moreover, it promotes surface-induced capacitive charge storage which, on one hand, provides a fast charge transfer improving the rate performance and causes less volume changes during de-/lithiation leading to an improved cycling stability on the other. Besides the above factors, also the carbon in V_2O_3/C has a beneficial impact on the electrochemical properties. It improves the electronic con-

ductivity and structural stability of the electrode material by providing a conductive backbone, which enhances the charge transfer, buffers the large volume changes during de-/lithiation, and hinders the self-aggregation of V_2O_3 nanostructures. This results in a high rate capacity and good cycling stability.

4. Conclusion

In summary, we demonstrate a facile hydrothermal thermolysis synthesis route to produce hierarchically structured porous V_2O_3/C microspheres. In this synthesis method, vanadyl hydroxide acts as precursor and different carboxylic acids as both the carbon source and reducing agents. The carbon content and specific surface area of the resulting V_2O_3/C nanocomposites can be controlled by varying the used carboxylic acid. In addition, the as-prepared products possess either core-shell or solid structure depending on the used carboxylic acid. Due to their special architecture, the V_2O_3/C composites exhibit very good electrochemical performance as anodes for LIBs, including high capacities and excellent cycling stabilities and rate capabilities. The high specific surface area facilitates a fast and less destructive capacitive charge storage contributing to superior electrochemical properties compared to chunk-like V_2O_3/C. Moreover, the carbon as conductive framework can effectively enhance the materials conductivity as well as the structural stability of the electrode material.

Declaration of Competing Interest

The authors declare that they have no known competing financial interests or personal relationships that could have appeared to influence the work reported in this paper.

Credit authorship contribution statement

E. Thauer: Conceptualization, Methodology, Investigation, Writing – original draft, Visualization. **G.S. Zakharova:** Conceptualization, Methodology, Investigation, Writing – original draft, Visualization. **L.F. Deeg:** Investigation. **Q. Zhu:** Investigation. **R. Klingeler:** Conceptualization, Writing – review & editing, Supervision.

Acknowledgments

This work was supported by the Deutsche Forschungsgemeinschaft through projects KL 1824/12–1 and KL 1824/14–1. G.Z. acknowledges support of the state order via the Ministry of Science and High Education of Russia (Theme no. AAAA-A19–119031890025–9). Partial support by the BMWi through project 03ET6095C (HiKoMat) is acknowledged. The authors thank I. Glass for experimental support.

Supplementary materials

Supplementary material associated with this article can be found, in the online version, at doi:10.1016/j.electacta.2021.138881.

References

[1] J.B. Goodenough, K.S. Park, The Li-ion rechargeable battery: a perspective, J. Am. Chem. Soc. 135 (2013) 1167–1176, doi:10.1021/ja3091438.
[2] B. Scrosati, J. Garche, Lithium batteries: status, prospects and future, J. Power Sources 195 (2010) 2419–2430, doi:10.1016/j.jpowsour.2009.11.048.
[3] F. Cheng, J. Liang, Z. Tao, J. Chen, Functional materials for rechargeable batteries, Adv. Mater. 23 (2011) 1695–1715, doi:10.1002/adma.201003587.
[4] G. Zubi, R. Dufo-López, M. Carvalho, G. Pasaoglu, The lithium-ion battery: state of the art and future perspectives, Renew. Sustain. Energy Rev. 89 (2018) 292–308, doi:10.1016/j.rser.2018.03.002.
[5] N. Nitta, F. Wu, J.T. Lee, G. Yushin, Li-ion battery materials: present and future, Mater. Today 18 (2015) 252–264, doi:10.1016/j.mattod.2014.10.040.
[6] S. Goriparti, E. Miele, F. de Angelis, E. Di Fabrizio, R. Proietti Zaccaria, C. Capiglia, Review on recent progress of nanostructured anode materials for Li-ion batteries, J. Power Sources 257 (2014) 421–443, doi:10.1016/j.jpowsour.2013.11.103.
[7] L. Ji, Z. Lin, M. Alcoutlabi, X. Zhang, Recent developments in nanostructured anode materials for rechargeable lithium-ion batteries, Energy Environ. Sci. 4 (2011) 2682, doi:10.1039/c0ee00699h.
[8] P. Poizot, S. Laruelle, S. Grugeon, L. Dupont, J.M. Tarascon, Nano-sized transition-metal oxides as negative-electrode materials for lithium-ion batteries, Nature 407 (2000) 496–499, doi:10.1038/35035045.
[9] S. Fang, D. Bresser, S. Passerini, Transition metal oxide anodes for electrochemical energy Storage in lithium- and sodium-ion batteries, Adv. Energy Mater. 10 (2020) 1902485, doi:10.1002/aenm.201902485.
[10] Q. Zhang, J. Wang, J. Dong, F. Ding, X. Li, B. Zhang, S. Yang, K. Zhang, Facile general strategy toward hierarchical mesoporous transition metal oxides arrays on three-dimensional macroporous foam with superior lithium storage properties, Nano Energy 13 (2015) 77–91, doi:10.1016/j.nanoen.2015.01.029.
[11] X. Yan, F. Jiang, X. Sun, R. Du, M. Zhang, L. Kang, Q. Han, W. Du, D. You, Y. Zhou, A simple, low-cost and scale-up synthesis strategy of spherical-graphite/Fe_2O_3 composites as high-performance anode materials for half/full lithium ion batteries, J. Alloys Compd. 822 (2020) 153719, doi:10.1016/j.jallcom.2020.153719.
[12] X. Gu, J. Yue, L. Li, H. Xue, J. Yang, X. Zhao, General synthesis of MnOx (MnO_2, Mn_2O_3, Mn_3O_4, MnO) hierarchical microspheres as lithium-ion battery anodes, Electrochim. Acta 184 (2015) 250–256, doi:10.1016/j.electacta.2015.10.037.
[13] E. Thauer, X. Shi, S. Zhang, X. Chen, L. Deeg, R. Klingeler, K. Wenelska, E. Mijowska, Mn_3O_4 encapsulated in hollow carbon spheres coated by graphene layer for enhanced magnetization and lithium-ion batteries performance, Energy 217 (2021) 119399, doi:10.1016/j.energy.2020.119399.
[14] Y. Dong, R. Ma, M. Hu, H. Cheng, J.-.M. Lee, Y.Y. Li, J.A. Zapien, Polymer-pyrolysis assisted synthesis of vanadium trioxide and carbon nanocomposites as high performance anode materials for lithium-ion batteries, J. Power Sources 261 (2014) 184–187, doi:10.1016/j.jpowsour.2014.03.020.
[15] Y. Shi, Z. Zhang, D. Wexler, S. Chou, J. Gao, H.D. Abruña, H. Li, H. Liu, Y. Wu, J. Wang, Facile synthesis of porous V_2O_3/C composites as lithium storage material with enhanced capacity and good rate capability, J. Power Sources 275 (2015) 392–398, doi:10.1016/j.jpowsour.2014.10.175.
[16] C. Huan, X. Zhao, X. Xiao, Y. Lu, S. Qi, Y. Zhan, L. Zhang, G. Xu, One-step solvothermal synthesis of V_2O_3@C nanoparticles as anode materials for lithium-ion battery, J. Alloys Compd. 776 (2019) 568–574, doi:10.1016/j.jallcom.2018.10.323.
[17] J. Leng, H. Mei, L. Zhan, Y. Wang, S. Yang, Y. Song, V_2O_3 nanoparticles anchored onto the reduced graphene oxide for superior lithium storage, Electrochim. Acta 231 (2017) 732–738, doi:10.1016/j.electacta.2017.01.133.
[18] D. Adler, J. Feinleib, Semiconductor-to-metal transition in V_2O_3, Phys. Rev. Lett. 12 (1964) 700–703, doi:10.1103/PhysRevLett.12.700.
[19] B. Qi, H.P. Gunnlaugsson, S. Ólafsson, H.P. Gislason, E.B. Thorsteinsson, U.B. Arnalds, R. Mantovan, I. Unzueta l, D.V. Zyabkin, K. Ram, K. Johnston, P.B. Krastev, T.E. Mølholt, H. Masenda, A. Martín-Luengo, D. Naidoo, J. Schell, Metal-insulator transition in crystalline V_2O_3 thin films probed at atomic-scale using emission Mössbauer spectroscopy, Thin Solid Films 714 (2020) 138389, doi:10.1016/j.tsf.2020.138389.
[20] C. Grygiel, A. Pautrat, P. Rodière, Galvanomagnetic properties and noise in a barely metallic film of V_2O_3, Phys. Rev. B 79 (2009), doi:10.1103/PhysRevB.79.235111.
[21] Y. Zhong, M. Yang, X. Zhou, Z. Zhou, Structural design for anodes of lithium-ion batteries: emerging horizons from materials to electrodes, Mater. Horiz. 2 (2015) 553–566, doi:10.1039/C5MH00136F.
[22] M. Zheng, H. Tang, L. Li, Q. Hu, L. Zhang, H. Xue, H. Pang, Hierarchically nanostructured transition metal oxides for lithium-ion batteries, Adv. Sci. 5 (2018) 1700592 (Weinheim, Baden-Wurttemberg, Germany), doi:10.1002/advs.201700592.
[23] H. Yue, Q. Wang, Z. Shi, C. Ma, Y. Ding, N. Huo, J. Zhang, S. Yang, Porous hierarchical nitrogen-doped carbon coated $ZnFe_2O_4$ composites as high performance anode materials for lithium ion batteries, Electrochim. Acta 180 (2015) 622–628, doi:10.1016/j.electacta.2015.08.139.
[24] L. Zhou, K. Zhang, Z. Hu, Z. Tao, L. Mai, Y.M. Kang, S.-.L. Chou, J. Chen, Recent developments on and prospects for electrode materials with hierarchical structures for lithium-ion batteries, Adv. Energy Mater. 8 (2018) 1701415, doi:10.1002/aenm.201701415.
[25] J. Liu, G. Cao, Z. Yang, D. Wang, D. Dubois, X. Zhou, G.L. Graff, L.R. Pederson, J.G. Zhang, Oriented nanostructures for energy conversion and storage, ChemSusChem 1 (2008) 676–697, doi:10.1002/cssc.200800087.
[26] Y. Wang, H. Li, P. He, E. Hosono, H. Zhou, Nano active materials for lithium-ion batteries, Nanoscale 2 (2010) 1294–1305, doi:10.1039/c0nr00068j.
[27] Y.G. Guo, J.S. Hu, L.J. Wan, Nanostructured materials for electrochemical energy conversion and storage devices, Adv. Mater. 20 (2008) 2878–2887, doi:10.1002/adma.200800627.
[28] B. Xiao, B. Zhang, L. Tang, C. An, Z. He, H. Tong, W. Yu, J. Zheng, V_2O_3/rGO composite as a potential anode material for lithium ion batteries, Ceram. Int. 44 (2018) 15044–15049, doi:10.1016/j.ceramint.2018.05.134.
[29] W. Cheng, G. Zeng, M. Niederberger, Design of vanadium oxide core–shell nanoplatelets for lithium ion storage, J. Mater. Chem. A 3 (2015) 2861–2868, doi:10.1039/C4TA05495D.
[30] X. Ren, D. Ai, C. Zhan, R. Lv, F. Kang, Z.H. Huang, NaCl-template-assisted freeze-drying synthesis of 3D porous carbon-encapsulated V_2O_3 for lithium-ion battery anode, Electrochim. Acta 318 (2019) 730–736, doi:10.1016/j.electacta.2019.06.138.

[31] L. Xun, S. Gao, Y. Xu, X. Cheng, X. Zhang, H. Zhao, L. Huo, Synthesis of dandelion-like V_2O_3/C composite with bicontinuous 3D hierarchical structures as an anode for high performance lithium ion batteries, Ceram. Int. 44 (2018) 14128–14135, doi:10.1016/j.ceramint.2018.05.012.
[32] P. Yu, X. Liu, L. Wang, C. Tian, H. Yu, H. Fu, Urchin-like V_2 O_3 /C hollow nanosphere hybrid for high-capacity and long-cycle-life lithium storage, ACS Sustain. Chem. Eng. 5 (2017) 11238–11245, doi:10.1021/acssuschemeng.7b01640.
[33] Le Jiang, Y. Qu, Z. Ren, P. Yu, D. Zhao, W. Zhou, L. Wang, H. Fu, *In situ* carbon-coated yolk-shell V_2O_3 microspheres for lithium-ion batteries, ACS Appl. Mater. Interfaces 7 (2015) 1595–1601, doi:10.1021/am5070393.
[34] P. Liu, K. Zhu, Y. Xu, K. Bian, J. Wang, G. Tai, Y. Gao, H. Luo, L. Lu, J. Liu, Hierarchical porous intercalation-type V_2 O_3 as high-performance anode materials for Li-ion batteries, J. Chem. 23 (2017) 7538–7544, doi:10.1002/chem.201700369.
[35] E. Thauer, G.S. Zakharova, S.A. Wegener, Q. Zhu, R. Klingeler, Sol-gel synthesis of Li_3VO_4/C composites as anode materials for lithium-ion batteries, J. Alloys Compd. 853 (2021) 157364, doi:10.1016/j.jallcom.2020.157364.
[36] C. Tenailleau, E. Suard, J. Rodriguez-Carvajal, M.P. Crosnier-Lopez, P. Lacorre, Effect of Mo doping on the room-temperature structure of vanadium sesquioxide, Chem. Mater. 14 (2002) 3569–3575, doi:10.1021/cm021127l.
[37] A.C. Ferrari, D.M. Basko, Raman spectroscopy as a versatile tool for studying the properties of graphene, Nat. Nanotechnol. 8 (2013) 235–246, doi:10.1038/NNANO.2013.46.
[38] N. Kuroda, H.Y. Fan, Raman scattering and phase transitions of V_2O_3, Phys. Rev. B 16 (1977) 5003–5008, doi:10.1103/PhysRevB.16.5003.
[39] Y. Ding, X. Xia, W. Chen, L. Hu, L. Mo, Y. Huang, S. Dai, Inside-out Ostwald ripening: a facile process towards synthesizing anatase TiO_2 microspheres for high-efficiency dye-sensitized solar cells, Nano Res. 9 (2016) 1891–1903, doi:10.1007/s12274-016-1081-2.
[40] L. Zhang, J. Yao, F. Xia, Y. Guo, C. Cao, Z. Chen, Y. Gao, H. Luo, VO_2 (D) hollow core–shell microspheres: synthesis, methylene blue dye adsorption and their transformation into C/VO x nanoparticles, Inorg. Chem. Front. 5 (2018) 550–558, doi:10.1039/C7QI00819H.
[41] J. Widoniak, S. Eiden-Assmann, G. Maret, Synthesis and characterisation of monodisperse zirconia particles, Eur. J. Inorg. Chem. 2005 (2005) 3149–3155, doi:10.1002/ejic.200401025.
[42] K.S.W. Sing, Reporting physisorption data for gas/solid systems with special reference to the determination of surface area and porosity (Recommendations 1984), Pure Appl. Chem. 57 (1985) 603–619, doi:10.1351/pac198557040603.
[43] A. Ottmann, M. Scholz, M. Haft, E. Thauer, P. Schneider, M. Gellesch, C. Nowka, S. Wurmehl, S. Hampel, R. Klingeler, Electrochemical magnetization switching and energy storage in manganese oxide filled carbon nanotubes, Sci. Rep. 7 (2017) 13625, doi:10.1038/s41598-017-14014-7.
[44] H. Li, P. Balaya, J. Maier, Li-storage via heterogeneous reaction in selected binary metal fluorides and oxides, J. Electrochem. Soc. 151 (2004) A1878, doi:10.1149/1.1801451.
[45] A. Tranchant, R. Messina, J. Perichon, Mechanism of electrochemical reduction of vanadium oxides, J. Electroanal. Chem. Interf. Electrochem. 113 (1980) 225–232, doi:10.1016/S0022-0728(80)80023-4.
[46] Y. Wang, H.J. Zhang, A.S. Admar, J. Luo, C.C. Wong, A. Borgna, J. Lin, Improved cyclability of lithium-ion battery anode using encapsulated V_2O_3 nanostructures in well-graphitized carbon fiber, RSC Adv. 2 (2012) 5748, doi:10.1039/c2ra20472j.
[47] G.S. Zakharova, E. Thauer, A.N. Enyashin, L.F. Deeg, Q. Zhu, R. Klingeler, V_2O_3/C composite fabricated by carboxylic acid-assisted sol–gel synthesis as anode material for lithium-ion batteries, J. SolGel Sci. Technol. 98 (2021) 549–558, doi:10.1007/s10971-021-05523-z.
[48] P. Simon, Y. Gogotsi, B. Dunn, Materials science. Where do batteries end and supercapacitors begin? Science 343 (2014) 1210–1211 (New York, N.Y.), doi:10.1126/science.1249625.
[49] T. Zhang, L. Zhang, L. Zhao, X. Huang, W. Li, T. Li, T. Shen, S. Sun, Y. Hou, Free-standing, foldable V_2O_3/multichannel carbon nanofibers electrode for flexible Li-ion batteries with ultralong lifespan, Small 16 (2020) e2005302 (Weinheim an der Bergstrasse, Germany), doi:10.1002/smll.202005302.
[50] C.S. Liu, X. Ye, B. Zhou, X.Q. Zeng, J. Xu, Q.C. Xu, J. Li, 2D mesoporous nanomesh from N-doped carbon-encapsulated V_2O_3 nanowires as an anode for lithium-ion batteries, J. Phys. Chem. C 124 (2020) 24073–24080, doi:10.1021/acs.jpcc.0c06899.
[51] L. Meng, R. Guo, F. Li, Y. Ma, J. Peng, T. Li, Y. Luo, Y. Li, X. Sun, Facile synthesis of flock-like V_2O_3 /C with improved electrochemical performance as an anode material for li-ion batteries, Energy Technol. 8 (2019) 1900986, doi:10.1002/ente.201900986.
[52] J. Liu, J. Liang, C. Wang, J. Ma, Electrospun CoSe@N-doped carbon nanofibers with highly capacitive Li storage, J. Energy Chem. 33 (2019) 160–166, doi:10.1016/j.jechem.2018.09.006.
[53] J. Yin, P. Sun, G. Qu, G. Xiang, P. Hou, X. Xu, A new CoO/Co_2B/rGO nanocomposite anode with large capacitive contribution for high-efficiency and durable lithium storage, Appl. Surf. Sci. 508 (2020) 144698, doi:10.1016/j.apsusc.2019.144698.
[54] X. Li, J. Fu, Z. Pan, J. Su, J. Xu, B. Gao, X. Peng, L. Wang, X. Zhang, P.K. Chu, Peapod-like V_2O_3 nanorods encapsulated into carbon as binder-free and flexible electrodes in lithium-ion batteries, J. Power Sources 331 (2016) 58–66, doi:10.1016/j.jpowsour.2016.09.031.